Journal of Alloys and Compounds 1057 (2026) 186733

Contents lists available at ScienceDirect

Journal of Alloys and Compounds

journal homepage: www.elsevier.com/locate/jalcom

Promoting in-situ martensite decomposition in PBF–LB α+β Ti alloys by Mn addition

Takuma Teramae [a,b,*], Johannes Wild [c,d], Jeff Huang [b], Delphine Chassaing [d,e], Ammarueda Issariyapat [b], Michael Konrad Eusterholz [c,d], Shota Kariya [b], Junko Umeda [b], Katsuyoshi Kondoh [b,**]

[a] Graduate School of Engineering, The University of Osaka, 2-1 Yamadaoka, Suita, Osaka 565-0871, Japan
[b] Joining and Welding Research Institute, The University of Osaka, 11-1 Mihogaoka, Ibaraki, Osaka 567-0047, Japan
[c] Institute for Applied Materials (IAM-WK), Karlsruhe Institute of Technology (KIT), Engelbert-Arnold-Str. 4, Karlsruhe 76131, Germany
[d] Karlsruhe Nano Micro Facility (KNMFi), Karlsruhe Institute of Technology (KIT), Hermann-von-Helmholtz-Platz 1, Eggenstein-Leopoldshafen 76344, Germany
[e] Institute of Nanotechnology (INT), Karlsruhe Institute of Technology (KIT), Hermann-von-Helmholtz-Platz 1, Eggenstein-Leopoldshafen 76344, Germany

ARTICLE INFO

Keywords:
Alloy design
Laser powder bed fusion
Martensite decomposition
Titanium alloys
Tensile Properties

ABSTRACT

Powder Bed Fusion–Laser Beam (PBF–LB) enables the fabrication of complex geometries but usually produces undesirable α′ martensitic microstructures in α+β Ti alloys. To address this issue through alloy design, we investigated the effect of Mn on the facilitation of in-situ martensite decomposition. As-built Ti-2Mn developed α+β microstructures at lower volumetric energy densities (VEDs) than as-built Ti-6Al-4V, despite their comparable β stability at martensite decomposition temperatures. Moreover, in Ti-2Mn, the α phase showed partial Mn depletion at a VED of 152 J/mm^3 and nearly reached equilibrium in Mn content at a VED of 357 J/mm^3. Meanwhile, Ti-6Al-4V retained an intermediate V content in the α phase between the equilibrium and α′ martensite states, even at 357 J/mm^3. Due to the facilitated martensite decomposition, the uniform elongation of Ti-2Mn improved from 6.3 % to 7.8 %, while its ultimate tensile strength decreased only slightly (928–857 MPa). Although its strength was lower than that of Ti-6Al-4 V, Ti-2Mn still achieved approximately 2.5-times higher strength than as-built commercially pure Ti while maintaining sufficient ductility without post-heat treatment. These results demonstrate that Mn addition provides a practical alloy-design strategy for enabling in-situ formation of α+β microstructures in PBF–LB Ti alloys, offering a complementary pathway to conventional process-parameter-based microstructure control.

1. Introduction

Metal additive manufacturing (MAM) has been widely used in various applications, including biomedical devices, aerospace components and automotive parts [1,2]. This widespread adoption is attributed to the high degree of freedom of MAM, which enables the fabrication of advanced components with complex geometries such as tailor-made and generative-artificial-intelligence aided designs [3,4]. Among the various MAM techniques, powder bed fusion-laser beam (PBF–LB) has received particular attention in industrial applications and academic research due to its excellent dimensional precision and flexibility in producing intricate structures [5,6]. These advantages arise from the layer-wise selective melting and solidification of a powder bed under controlled laser irradiation. However, the extremely high cooling rates involved (10^6–10^7 °C/s [7]) often lead to the formation of fully martensitic α′ microstructures in Ti alloys [8].

Titanium alloys are generally classified into α, α+β, and β types based on their phase constitution. The α+β alloys consist of an α phase with a hexagonal close-packed (hcp) structure and a β phase with a body-centered cubic (bcc) structure. Their dual-phase microstructures form through a diffusion-controlled allotropic transformation and are retained by adequate amounts of β-stabilizing elements, such as V in Ti-6Al-4V. Under conventional processing, α+β microstructures are typically obtained unless suppressed by rapid cooling techniques such as water quenching (>410 °C/s) [9]. In contrast, PBF-LB imposes much higher cooling rates (10^6–10^7 °C/s [7]), which typically lead to the

* Corresponding author at: Graduate School of Engineering, The University of Osaka, 2-1 Yamadaoka, Suita, Osaka 565-0871, Japan.
** Corresponding author.
E-mail addresses: teramae.takuma.f1a@ecs.osaka-u.ac.jp (T. Teramae), kondoh.katsuyoshi.jwri@osaka-u.ac.jp (K. Kondoh).

https://doi.org/10.1016/j.jallcom.2026.186733
Received 11 September 2025; Received in revised form 9 January 2026; Accepted 8 February 2026
Available online 9 February 2026

formation of metastable α′ martensite.

The α′ martensite is a non-equilibrium α phase produced through a diffusionless martensitic transformation. This transformation generates a distinctive lath-type microstructure and leaves β stabilizing elements supersaturated within the α matrix, as no solute partitioning occurs during the rapid transformation. To restore such martensite to the desired α+β microstructures, as-built components usually undergo post-heat treatment [10–12], which enable the supersaturated β stabilizers to diffuse into α lattice defects and nucleate the β phase [13].

Alternatively, by utilizing an intrinsic heat treatment (IHT) effect, the equilibrium α+β microstructures can be obtained in as-built conditions [14]. The IHT phenomenon occurs due to the heat accumulation in the components during building. Thus, although martensite is inevitably formed, it may be subsequently decomposed into the α+β phases over the course of a PBF–LB process, i.e., in-situ martensite decomposition. To reliably control this IHT-driven microstructure manipulation, various strategies have been attempted in Ti-6Al-4V, such as support structure optimization [15], a component layout design [16] and process parameter optimization [14,15,17–22]. In particular, Ter Haar and Becker demonstrated that reduced scan speeds and hatch distances promoted in-situ martensite decomposition [20]. Furthermore, the application of high laser power effectively resulted in the in-situ formation of various α+β microstructures [23]. However, many process parameters (such as laser power, focal offset, or baseplate temperature) are constrained by machine specifications, motivating the exploration of complementary strategies.

Alloy design has been achieving various microstructure manipulation in as-built conditions, such as grain refinement, columnar to equiaxed transition (CET), and phase transition [24,25]. This strategy has the advantage of being less constrained by process parameter adjustability, because it relies on customized feedstock chemistry. However, there are only a few reports addressing in-situ martensite decomposition through alloy design [26]. In the literature, a part of V in Ti-6Al-4V were replaced by Fe via in-situ alloying approach, facilitating the formation of α+β microstructures during PBF–LB [26]. Although the exact mechanism remains unclear, the diffusivity of Fe is believed to play a vital role in the martensite decomposition. Because Fe exhibits abnormally fast diffusion in the α phase [27], it may accelerate β phase nucleation more effectively than V, thereby facilitating α+β microstructure formation. However, the effect of other fast diffusive solutes on in-situ martensite decomposition remains unexplored.

To identify promising solutes for this purpose, our previous study systematically examined the kinetics of martensite decomposition among several α+β Ti alloys each containing Mn, Fe, Cr, and V under equivalent β stability set through CALPHAD-aided composition design [28]. This comparison indicated that Mn, owing to its relatively fast diffusivity, promotes earlier martensite decomposition than V. However, because that study relied on powder metallurgy and post-heat treatment to isolate chemical effects, the effectiveness of Mn under actual PBF–LB conditions has not yet been fully established.

In this study, we investigated the crystallographic characteristics and mechanical properties of a binary Ti-Mn alloy fabricated by PBF–LB and compared them with those of a Ti-6Al-4V alloy with a focus on in-situ martensite decomposition. The Mn content of the alloy was first set based on equivalency of equilibrium β phase fraction of Ti-Mn to Ti-6Al-4V. Both alloys were then fabricated by PBF–LB with various scan speeds and hatch distances to induce the different degrees of IHT. Their microstructures, phase constitutions, nanoscale solute distributions, and mechanical properties were subsequently characterized to assess the role of Mn in facilitating in-situ martensite decomposition during PBF–LB.

2. Methodology

2.1. CALPHAD

By using a CALPHAD approach (CALculation of PHAse Diagrams), the Mn content for the alloy was set to be 2 wt%. The calculation was conducted in the Pandat software, employing two databases: the Computational Phase Diagram Database (CPDD, National Institute for Materials Science) for a Ti-Mn system [29,30] and the PanTitanium thermodynamic database (CompuTherm LLC) for a Ti-6Al-4V alloy [31]. As shown in Fig. 1, the systems of Ti-2Mn and Ti-6Al-4V exhibited similar β phase fraction curves particularly at 550–682℃, which is a critical range in the present study. Although martensite decomposition in Ti-6Al-4 V has been reported to occur between 423 and 682℃ [32], Ti-2Mn undergoes a eutectoid reaction forming a mixture of α-Ti and α(Ti, Mn) below 550℃ [33]. This study therefore focused on the range of 550–682℃ (highlighted in Fig. 1) to examine decomposition especially into the α+β phases. Within this range, the difference in β phase fraction between the two alloys is small (0.01–0.05), indicating comparable β stability, as shown in the magnified panel in Fig. 1.

The Gibbs free energy was also calculated to compare the chemical driving force for martensite decomposition, ΔG_{chem}, between Ti-2Mn and Ti-6Al-4V:

$$\Delta G_{chem} = G_{\alpha+\beta} - G_{\alpha'} \quad (1)$$

Here, $G_{\alpha+\beta}$ and $G_{\alpha'}$ denote the Gibbs free energy under equilibrium α+β and non-equilibrium α′ conditions, respectively. $G_{\alpha+\beta}$ was obtained using the lever rule by weighting the Gibbs energies of each solute-partitioned phase by their respective equilibrium phase fractions. $G_{\alpha'}$ was calculated by assuming that all solute elements remain in a single α phase without partitioning, consistent with α′ being a supersaturated α phase formed through diffusionless martensitic transformation.

The time-dependent evolution of β phase volume fraction was further calculated to compare the β evolution behaviours between Ti-2Mn and Ti-6Al-4V using the PanEvolution module coupled with the Pandat software [34]. The simulation employed a KWN (Kampmann-Wagner Numerical) model, incorporating the α and β phases as matrix and precipitate, respectively. Since these phases satisfy the Burgers orientation relationship, the interface is coherent during the early stages of precipitation [35,36]. Accordingly, the interfacial energy was set to 0.04 J/mm^2, assuming the coherent interface based on a previous report [37]. Besides, grain boundaries were assigned as nucleation sites, reflecting the characteristics of the samples in this study.

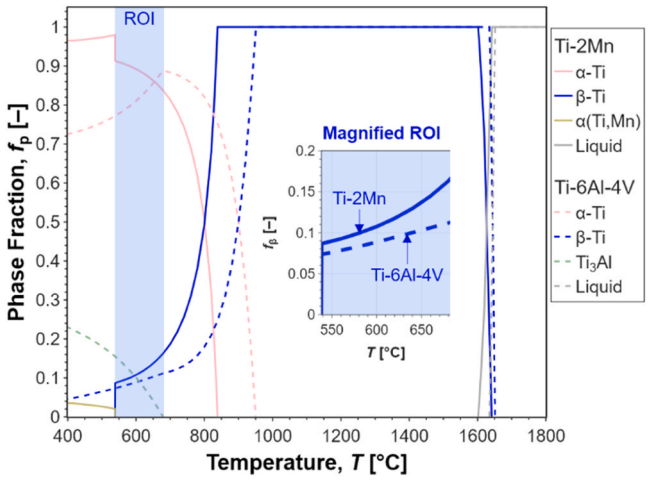

Fig. 1. Equilibrium phase fraction curves of Ti-2Mn and Ti-6Al-4V estimated by CALPHAD.

2.2. Materials

To prepare the feedstock for a Ti-2Mn alloy, commercially pure (CP) Ti and Mn powders were employed. The Ti powder supplied by Osaka Titanium Technologies Co., Ltd. showed a spherical morphology with characteristic diameters of D_{10}= 23.8, D_{50} = 33.7, D_{90}= 49.1 μm and a purity of 99.89 % (Fig. 2(a-1 and b-1)). The Mn powder supplied by Kojundo Chemical Laboratory Co., Ltd. showed an irregular morphology with a particle size of D_{10}= 3.0, D_{50} = 5.4, D_{90}= 8.6 μm and a purity of 99.9 % (Fig. 2(a-2 and b-2)). These powders were filled in a polypropylene container with Ar gas and subsequently mixed using a rocking mill (RM-05, Seiwa Giken). The mixing was performed with zirconia balls (10 mm in diameter and 10:1 in a powder to ball weight ratio) for 1 h. As shown in Fig. 2(b-3), the mixed Ti-2Mn feedstock showed a homogeneous dispersion of Mn particles around Ti particles. For Ti-6Al-4V, a pre-alloyed powder supplied by Osaka Titanium Technologies Co., Ltd. was used, featuring a spherical morphology similar to the CP-Ti powder. Its characteristic diameters were D_{10}= 12.6, D_{50} = 25.4, D_{90}= 44.6 μm. The size distribution of all powders was obtained by laser diffraction analysis (LA-950, HORIBA).

The feedstocks of Ti-2Mn and Ti-6Al-4V were first built into 10 × 10 × 10 mm^3 blocks with contour-type support structures on a Ti baseplate using a PBF–LB machine (TruPrint1000, TRUMPF) with a laser beam diameter of 30 μm. The build chamber was purged with high purity Ar gas to maintain an oxygen concentration around 100 ppm. Schematics of the scanning strategy and build plate configuration are shown in Fig. 3(a). All blocks were built using the same chessboard scanning pattern, laser power (P = 200 W), and layer thickness (t = 20 μm). Meanwhile, different scan speeds (v = 400–660 mm/s) and hatch spacings (h = 70–100 μm) were applied to vary the volumetric energy densities (VEDs), E_V, defined as follows:

$$E_V = \frac{P}{vht} \tag{2}$$

The applied E_V was in the range of 152–357 J/mm^3 as indicated in Fig. 3(b).

This range was validated by the sufficiently low porosity, which remained below 0.20 % and 0.21 % for Ti-2Mn and Ti-6Al-4V, respectively (Fig. S1 (a) in the supplementary material). In addition, most pores were spherical (Fig. S1(b)), suggesting negligible influence on mechanical properties based on previously reported relationships for Ti-6Al-4 V [38].

Moreover, within this VED range, the difference in feedstock type, i.e., pre-mixed vs. pre-alloyed powder, was regarded as insignificant based on SEM-EDS analysis (supplementary material). This note shows that Ti-2Mn fabricated from mechanically mixed powders exhibited only minor Mn segregation at 152 J/mm^3 , with a statistical distribution comparable to that of V in pre-alloyed Ti-6Al-4 V. Although a small Mn loss (~0.3 wt%) occurred at higher VED, the overall Mn content remained close to the nominal 2 wt%, indicating that elemental homogeneity and post-build composition were sufficiently maintained for subsequent microstructural comparison.

After processing, specimens for characterization were extracted 3 mm from the top surface of build blocks using wire electric discharge machining (WEDM). This sectioning strategy was adopted to eliminate the influence of microstructural heterogeneity along the z-axis (vertical direction) when comparing between Ti-2Mn and Ti-6Al-4V, particularly for microstructure observation and X-ray diffraction (XRD) analysis [17,18,26].

Second, based on the characteristics of these block-shaped samples, the VEDs of 152 and 357 J/mm^3 were selected for further analysis of microstructures and elemental partitioning in the nanoscale and to characterize mechanical properties. Bars with dimensions of 10 × 50 × 10 mm^3 were subsequently built from the Ti-2Mn and Ti-6Al-4V feedstocks (Fig. 4). This process was conducted with the same interlayer time (51 s) as the fabrication of block-shaped samples, ensuring an identical thermal window for microstructure evolution during IHT. After fabrication, each bar was removed from the baseplate and processed into six tensile specimens at 0.5 mm intervals by WEDM. Each specimen featured a rectangular gauge cross-section of 1 × 2 mm, and a reduced section length of 10 mm.

2.3. Characterization

The xy plane (horizontal plane) of sectioned specimens was mechanically polished with SiC abrasive papers and then finished by a vibratory polishing with a colloidal silica suspension to obtain a mirror surface. The polished surface was observed by a light optical microscope (OM, DSX, Olympus) to evaluate porosity. Bright field images with a resolution of 2.2 μm/pixel were obtained and analysed by software, ImageJ [39]. By applying auto thresholding using the intermodes method [40], the bright field images were binarized, followed by the quantification of the area fraction of pores. To investigate microstructures, a scanning electron microscope (SEM, JSM-7100F, JEOL) operating at 15 kV was used in backscattered electron (BSE) mode. To compare the microstructures in Ti-2Mn and Ti-6Al-4V prepared across the various processing parameters, at least 15 BSE images were randomly obtained from each sample. Based on microstructural features (see in Section 3.1), the obtained BSE images were categorized into three groups: martensitic, near-martensitic, and decomposed. For each sample, the number of images in each group was counted and divided by the total number of images, which is referred to as the classification rate.

XRD analysis was performed with Cu-Kα radiation (λ = 0.154 nm) at room temperature using a Bragg-Brentano configuration (LabX XRD-6100, Shimadzu). Tube voltage and current were set to 40.0 kV and 30.0 mA, respectively. Both divergence and scattering slits were set to 1.0 deg. The receiving slit was 0.15 mm. The scanning speed, step size, and sampling range were set to 0.5 deg/min, 0.02 deg, and 20–90 deg, respectively. The obtained raw XRD profiles were indexed and analysed in Profex software, with reference data from the Crystallography Open Database (COD) [41,42]. Whole pattern fitting was performed using the Le Bail method to obtain the lattice parameters. It should be noted that the XRD profiles shown in this article were smoothed by the Savitzky-Golay filter [43] to reduce the noise and support the visibility of signals with low intensity. The smoothing was performed using the 'savgol_filter' function from the 'scipy.signal' module in Python with a window length of 15 and polynomial order of 2. To support interpretation of the lattice parameter evolution, the O and N contents were measured by inert gas fusion analysis (EMGA-830, HORIBA).

The microstructures of the bar samples were further investigated using a transmission electron microscope (TEM, JEM-2100F, JEOL) operating at 200 kV. The distribution of phases and alloying elements were analysed by the selected area electron diffraction (SAED) patterns and energy-dispersive X-ray spectroscopy (EDS). The TEM foils were prepared using a focused ion beam (MultiBeam FIB system, JIB-4500) incorporated in an SEM operated at 30 kV. Moreover, atom probe tomography (APT) was employed for quantitative evaluation of elemental partitioning. Needle-shaped APT specimens were extracted by a SEM-FIB (Auriga 60, Zeiss) with a BSE detector. Prepared specimens were analysed with a Cameca local electrode atom probe (LEAP, 4000X HR) at a base temperature of 50 K. The laser mode was used at a laser energy of 50 pJ, a pulse rate of 200 kHz, and a detection rate of 0.3 %. Using the APT Suite software 6.3 (CAMECA/AMETEK), obtained APT mass spectra were indexed and identified with elements of Mn, Al, V, Fe, O, N, and C, which were selected based on the certificates of chemical composition of each raw powder provided by suppliers.[1] Note that the indexing and

[1] Mn was considered specifically for Ti-2Mn, whereas Al and V were assessed for Ti-6Al-4V. In contrast, O, N, Fe, and C were analyzed across all samples because these elements are intrinsic impurities commonly present in both CP-Ti and Ti-6Al-4V feedstocks.

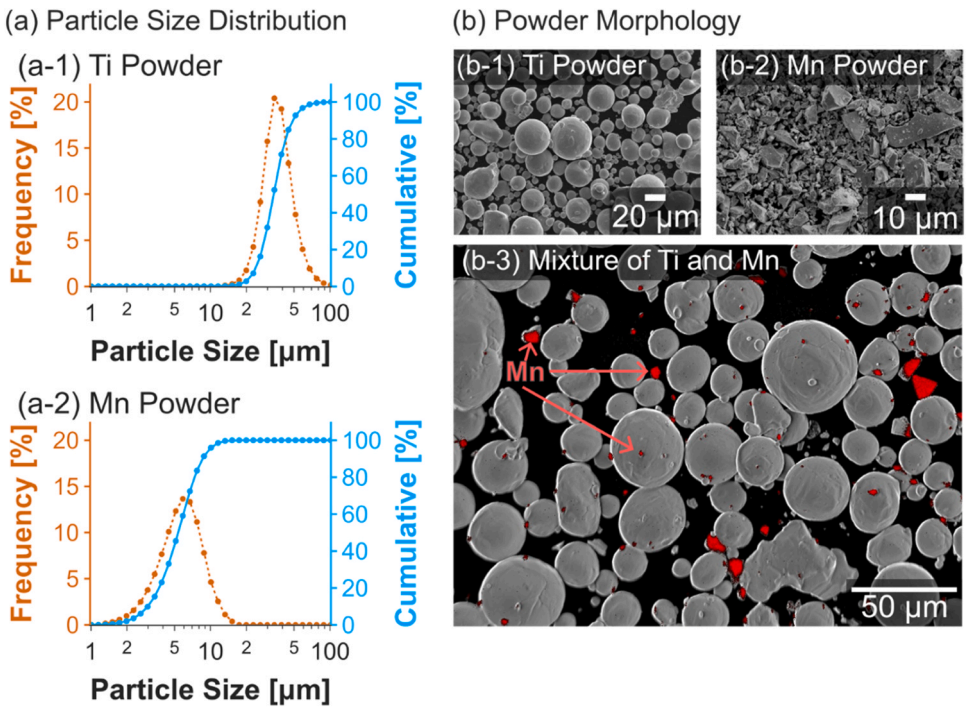

Fig. 2. Characteristics of feedstock for a Ti-2Mn alloy: (a) particle size distribution and (b) powder morphology. Note that (b-3) displays a secondary electron image of the mixture of Ti and Mn powder overlayed with an EDS count map of Mn (red color).

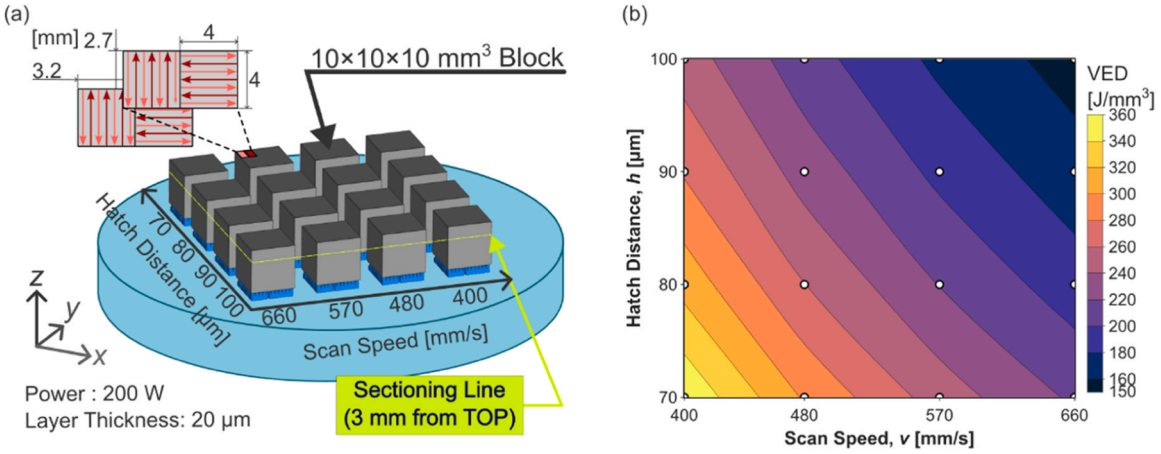

Fig. 3. (a) Build plate configuration, parameters, and scan strategy. (b) the corresponding volumetric energy density in the layout in (a).

identification were conducted on the basis of the natural isotope abundances of all ions containing these elements. Thereafter, the data were three-dimensionally reconstructed and quantitatively analysed. In this APT analysis, post heat treated Ti-2Mn and Ti-6Al-4V were also analysed for reference. The heat treatment parameters were set to 800℃ and 6 h in holding temperature and time, respectively, based on the report by Cao et al. [11].

To evaluate mechanical properties, uniaxial tensile testing was performed at room temperature using a universal testing machine (Autograph AG-X, Shimadzu) with an initial crosshead speed of 5.0×10^{-3} mm/s. Strain was measured using a non-contact digital video extensometer (TRViewX, Shimadzu). The fractured specimens were first analysed using OM to measure the reduction of area and were subsequently observed by SEM to investigate fracture surfaces.

3. Results and discussion

3.1. XRD analysis

The phase constitution and lattice parameters were analysed using XRD. Fig. 5 shows XRD profiles of Ti-2Mn and Ti-6Al-4V built with 152, 195, 260, and 357 J/mm^3. All patterns exhibited diffraction peaks of the α and β phases without any detectable peaks of intermetallic compounds such as α(Ti, Mn) and Ti_3Al. The β peaks exhibited low integrated intensity at low VEDs. For example, in Ti-2Mn, the proportion of the integrated intensity of β peaks was only 3.6 % of the total integral of all peaks at a VED of 152 J/mm^3, while it was 13.2 % at a VED of 357 J/mm^3. Although these values do not directly reflect the volume fraction of the β phase, the low integrated intensity semi-quantitatively indicates the presence of small amounts of β grains in Ti-2Mn and Ti-6Al-4V even at a VED of 152 J/mm^3.

Martensite decomposition is known to be accompanied by the

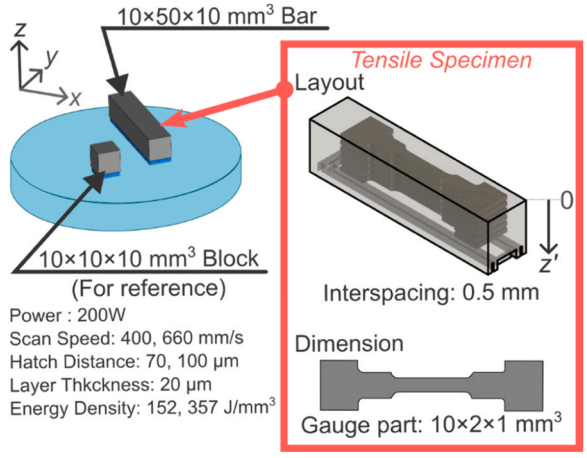

Fig. 4. Schematics of the building layout of a bar sample for tensile testing.

evolution of α lattice parameters [15,20,44]. Fig. 6 shows that the lattice parameter of the c-axis increased with VED, while the lattice parameter of the a-axis was almost insensitive to VED. This anisotropic expansion is commonly represented by an increase in the c/a ratio, reflecting the progression of martensite decomposition [15,20,44]. During decomposition, the α phase undergoes depletion of supersaturated β stabilizing elements. When the β stabilizers have smaller atomic size than Ti (e.g., Mn and V), this solute depletion causes the α lattice expansion. Moreover, the Mn and V solutes introduce a larger α lattice distortion along the c-axis than the a-axis [45]. Consequently, the c/a ratio increases as martensite decomposition progresses.

As pointed out in the literature [20], the influences of O and N should be also considered in discussing the evolution of α lattice parameters. These elements can be easily picked up during the PBF–LB process due to their high reactivity with Ti. This contamination may occur even though the processing chamber is purged with an Ar atmosphere with a low O content (around 100 ppm) [20,46]. Since O and N primarily occupy interstitial octahedral sites in the HCP α phase, their solid solution also produces an anisotropic lattice expansion to the c-axis [47]. Thus, in this study, the influences of O and N were estimated using the previously reported relationship between O/N contents in CP-Ti and the lattice parameter of the c-axis [48,49].

The O and N contents measured by inert gas fusion and their estimated influences on the lattice parameter of the c-axis are summarized in Fig. 7. The O content was almost insensitive to VED in Ti-2Mn but slightly increased in Ti-6Al-4V. In both alloys, the N content increased with VED. Despite these increases, their influences on the lattice parameter appeared to be limited on the basis of their slopes of linear regression drawn in Fig. 7. Namely, whereas the slopes of the estimated

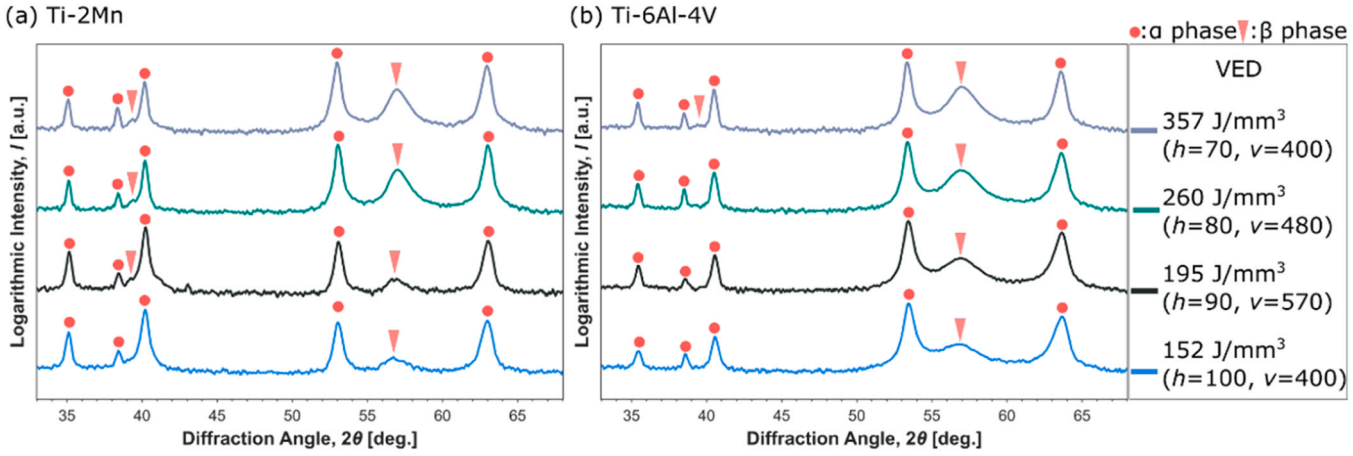

Fig. 5. XRD profiles of (a) Ti-2Mn and (b) Ti-6Al-4V built with various VEDs: 152 J/mm^3, 195 J/mm^3, 260 J/mm^3, and 357 J/mm^3.

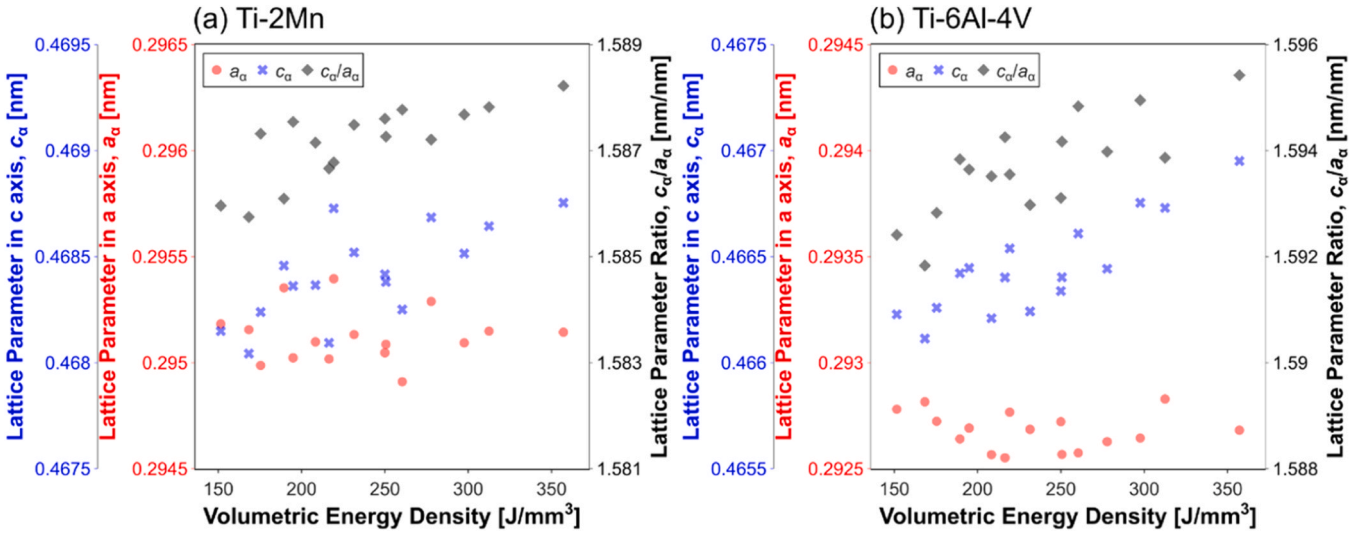

Fig. 6. Lattice parameter evolution of the α phase in (a) Ti-2Mn and (b) Ti-6Al-4V, including lattice parameters in a- and c-axes and their ratio.

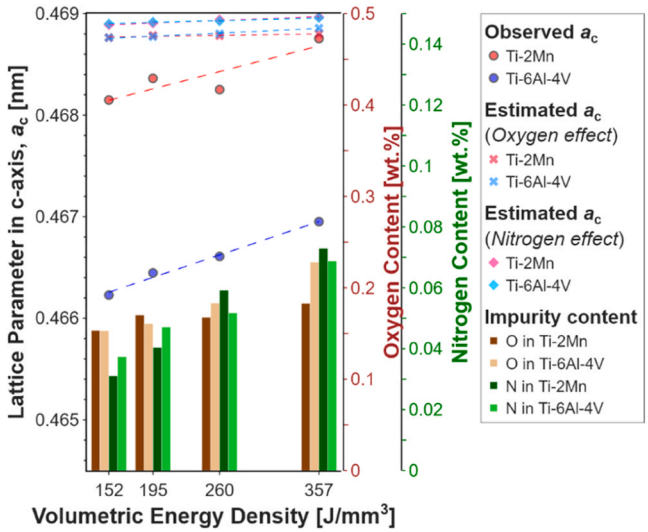

Fig. 7. Influence of impurity O and N contents on the α lattice parameter in c-axis. Scatter plots present the observed (indicated by circle) and estimated (indicated by cross and diamond) lattice parameters, while bar plots show the measured O and N content.

lattice parameters with respect to the VED were 1.6–4.7 × 10^{-7}, the slopes of the observed lattice parameters were 2.6 × 10^{-6} and 3.4 × 10^{-6} for Ti-2Mn and Ti-6Al-4V, respectively. Thus, O and N contamination contributed only about 10 % of the observed lattice expansion in both alloys.

Moreover, it is worth noting that the observed and estimated lattice parameters of Ti-2Mn were in good agreement at the VED of 357 J/mm^3, while those of other Ti-2Mn were overestimated. This behaviour indicates that the α phase in Ti-2Mn built at 152, 195, and 260 J/mm^3 remains in a martensitic (supersaturated) state, while the α phase at 357 J/mm^3 is no longer martensitic but instead approaches an equilibrium α composition due to substantial Mn depletion. Note that the large overestimation observed for Ti-6Al-4 V was attributed to the influence of Al on the lattice parameter, which was not considered in the estimation based on CP-Ti. In fact, Al solutes decrease the lattice parameter owing to their smaller atomic size relative to Ti [50]. Thus, the observed lattice parameter cannot be directly compared with the estimated values in Ti-6Al-4 V, and no inference is made regarding the α-phase state in this alloy. Nevertheless, this limitation does not compromise the validity of the preceding slope-based analysis.

3.2. SEM observations

To understand microstructural evolution with an increase in VED, Fig. 8 shows BSE images of Ti-2Mn and Ti-6Al-4V built under four different conditions of VED: 152, 195, 260 and 357 J/mm^3. At the lowest VED of 152 J/mm^3, both alloys exhibited typical martensitic microstructures, identified by martensitic lath boundaries and twins (Fig. 8(a-1, b-1)). At 195 J/mm^3, Ti-2Mn partially showed distinct β grains between α grains in addition to the martensitic features (Fig. 8(a-2)), which is classified here as a near-martensitic microstructure. This microstructure represents a transitional state from fully martensitic α′ to decomposed α+β. In contrast to Ti-2Mn, Ti-6Al-4V built with 195 J/mm^3 retained a similar martensitic microstructure to that observed with 152 J/mm^3 (Fig. 8(b-2)). A near-martensitic microstructure for Ti-6Al-4V was observed at 260 J/mm^3 (Fig. 8(b-3)). Finally, both alloys showed decomposed microstructures at 357 J/mm^3, where the α grains were almost fully surrounded by the β phase (Fig. 8(a-4, b-4)). This microstructural evolution was attributed to the elevated IHT temperature, which increase with VED as reported by Cobbinah et al. [51].

Since this evolution occurred only gradually with increasing VED

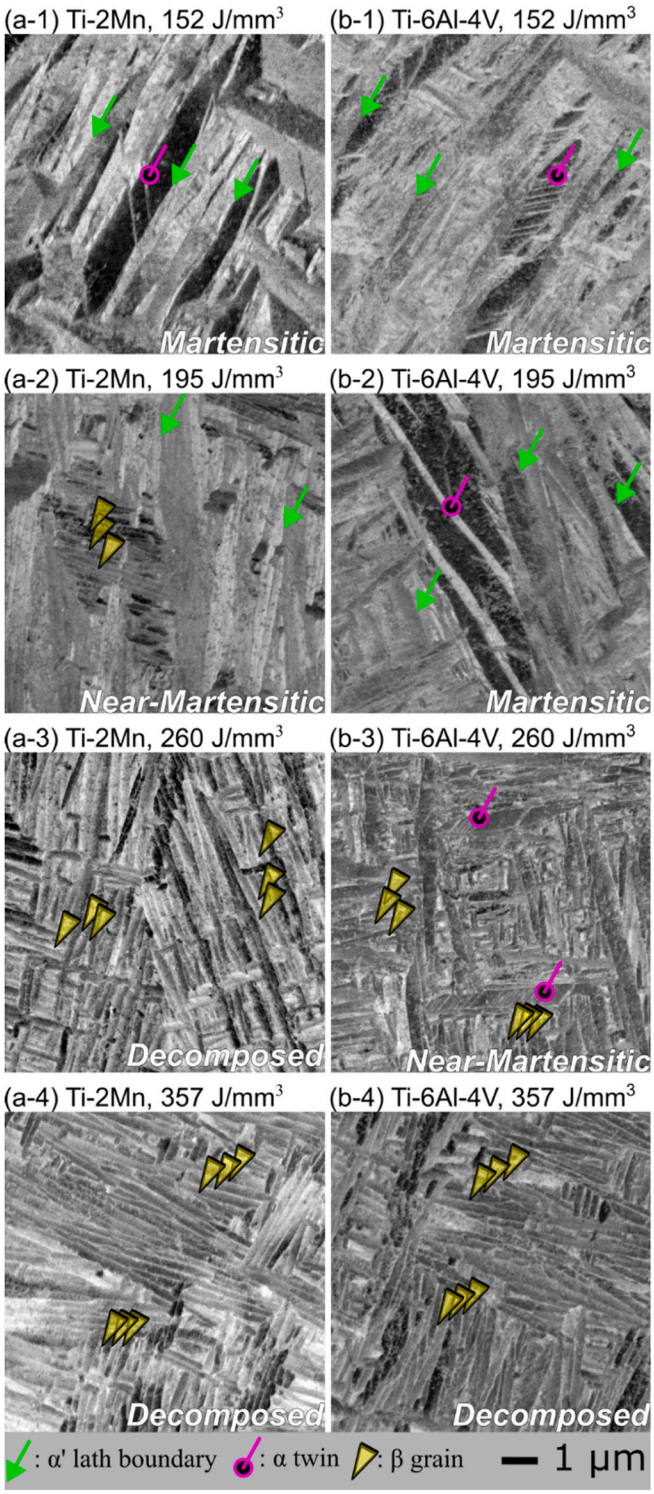

Fig. 8. BSE images of microstructures on the xy plane of (a) Ti-2Mn and (b) Ti-6Al-4V built with various VEDs: (1) 152 J/mm^3 (v = 660, h = 100), (2) 195 J/mm^3 (v = 570, h = 90), (3) 260 J/mm^3 (v = 480, h = 80), (4) 357 J/mm^3 (v = 400, h = 80).

(Fig. 8), residual martensitic α′ was still found even at the VED that predominantly exhibited the decomposed microstructures. To clarify the relationship between VEDs and microstructures, the number of BSE micrographs corresponding to each classification was counted and expressed as a percentage of all micrographs in each sample. As shown in Fig. 9(a), Ti-2Mn exhibited a transition in the predominant category

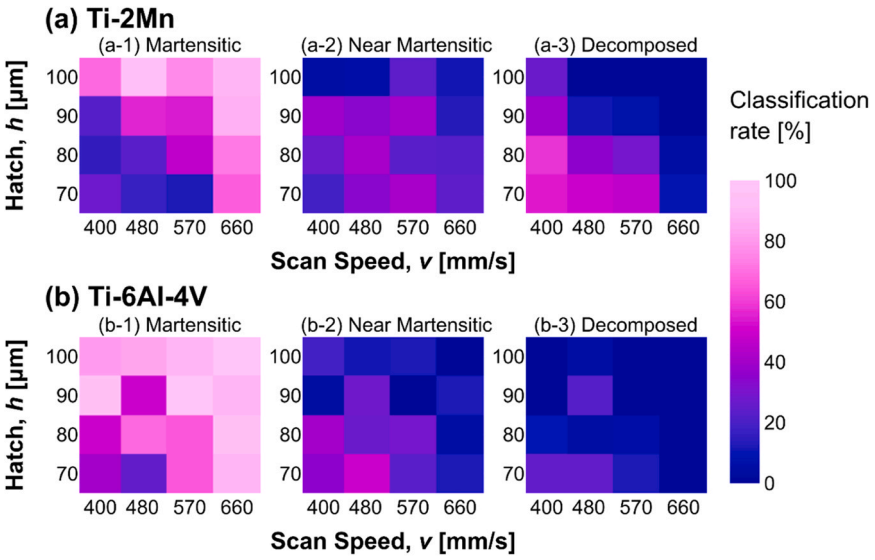

Fig. 9. Microstructure classification rates of (a) Ti-2Mn and (b) Ti-6Al-4V.

of microstructures, shifting from martensitic to decomposed ones as the hatch distance and scan speed decreased (i.e., with increasing VED). Meanwhile, even though Ti-6Al-4V exhibited the decomposed microstructures at the high VED (Fig. 8), the classification rate of decomposed microstructures remained remarkably low (Fig. 9(b)). Consequently, martensitic microstructures predominated in Ti-6Al-4V across almost all processing conditions. This difference in microstructural evolution between the two alloys indicates that in-situ martensite decomposition occurred more effectively in Ti-2Mn than in Ti-6Al-4 V.

3.3. TEM and APT analysis

To identify the β phase in microstructures, TEM analysis was conducted (Fig. 10). In SAED analysis of the interface between α grains, multiple sets of diffraction spots were observed in both Ti-2Mn and Ti-6Al-4V. These patterns were indexed to a mixture of the α and β diffraction spots. Dark field images taken using the β diffraction spots of 211 (Ti-2Mn) and 002 (Ti-6Al-4V) revealed distinct fine β grains located between α grains. This result, especially for Ti-6Al-4V, is in agreement with previous studies which revealed V enrichment in intergranular β grains by TEM and APT analyses [13,35]. For Ti-2Mn, the Mn distribution was investigated by EDS analysis. Fig. 11 (a, b) shows the fine intergranular β grains were enriched with Mn. Furthermore, the semi-quantitative analysis along an A-A′ line demonstrated that the local Mn content reached up to 10 at% at most in the β phase, whereas it was around 0.5 at% in the α phase.

The elemental distributions in Ti-2Mn and Ti-6Al-4V were quantified by APT. Fig. 12 (a) shows the 3D reconstruction of the analysed tip of Ti-2Mn built with 357 J/mm^3, confirming the presence of Mn-rich regions. These regions were also enriched in Fe and slightly depleted in O and N (indicated by triangles in Fig. 12 (a)). Based on the TEM analysis (Figs. 10 and 11), these Mn-rich regions correspond to the intergranular β phase. For a quantitative analysis, the iso-concentration surfaces of 3 at% Mn were drawn, and the corresponding proximity histogram (proxigram) was obtained (Fig. 12 (b and c)). The proxigram indicated that the mean Mn contents were 0.68 and 11.4 at% in the α and β phases, respectively, consistent with the semi-quantitative result from STEM-EDS (Fig. 11). It should be noted that the mean contents were

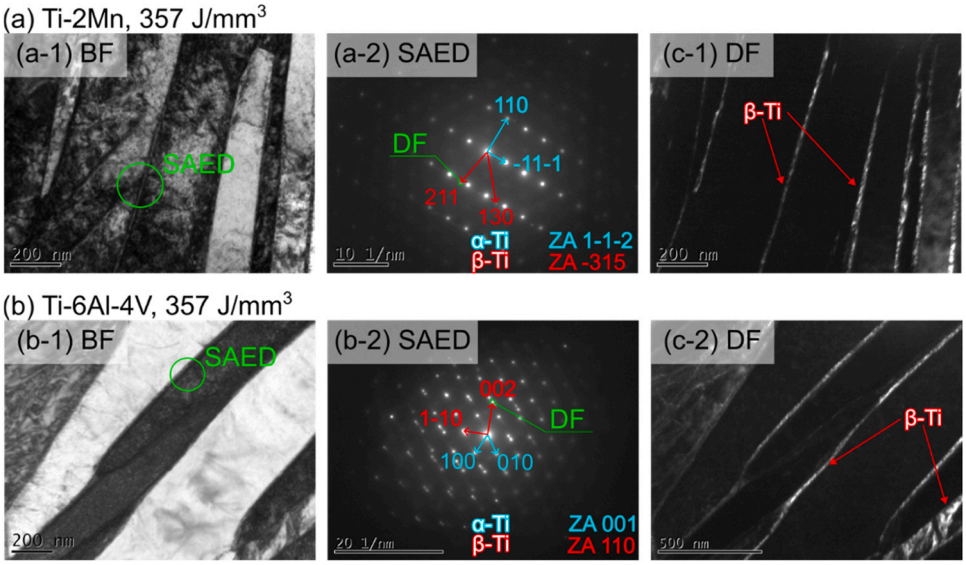

Fig. 10. TEM analysis on (a) Ti-2Mn and (b) Ti-6Al-4V built with the VED of 357 J/mm^3, including (1) bright-field (BF) images, (2) SAED patterns of circled region in (1), and (3) dark-field images of the same area corresponding to the circled diffraction spot in (2).

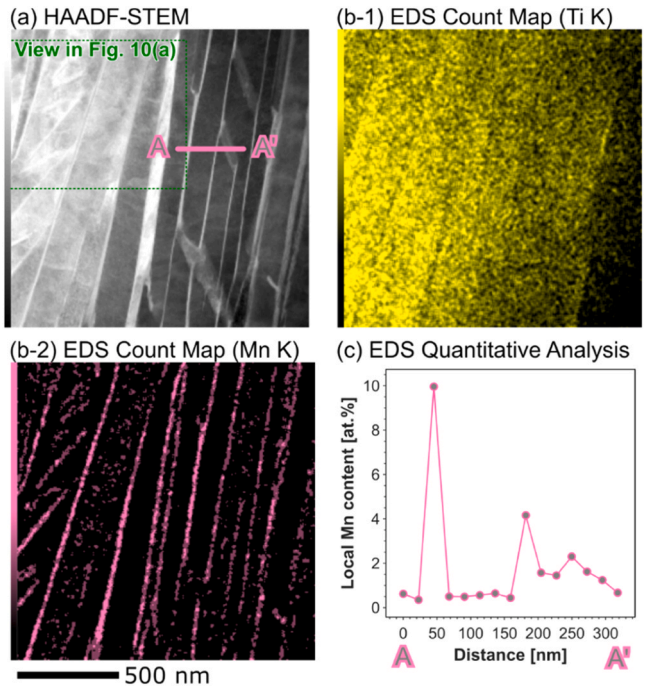

Fig. 11. STEM-EDS analysis on Ti-2Mn built with the VED of 357 J/mm^3, including (a) a high-angle annular dark-field (HAADF) image, (b) EDS count maps of (1) Ti and (2) Mn, and (c) semi-quantitative analysis of local Mn content along an A-A' line in (a).

calculated from plateau regions in each phase (highlighted in Fig. 12 (c)).

By applying the same quantification framework, the solute partitioning in other samples was also examined (Fig. 13). In all Ti-2Mn samples, the α phase contained significantly lower Mn contents than the nominal overall Mn content ($c_{\text{bulk, Mn}}$ =1.75 at%). The highest Mn content was measured at the VED of 152 J/mm^3 (1.0 at%), followed by the VED of 357 J/mm^3 (0.68 at%). Notably, although the further depletion was attempted by the post heat treatment (800°C, 6 h), the Mn content was only reduced to 0.48 at% because it approached the equilibrium solubility in the α phase ($c_{\text{sol, Mn}}$ = 0.4 at%) [33]. Therefore, the Mn content in the α phase was nearly at equilibrium at 357 J/mm^3 , whereas at 152 J/mm^3 it represented an intermediate value between the equilibrium and martensitic non-equilibrium states. This difference in Mn content is consistent with the preceding discussion regarding the overestimation and accurate estimation of the α lattice parameter at 152 and 357 J/mm^3 , respectively (Fig. 9).

In contrast to Ti-2Mn, Ti-6Al-4V did not exhibit remarkable V depletion from the α phase (Fig. 13 (b-1)). At a VED of 152 J/mm^3 , the α phase contained a high V content (3.9 at%), similar to the nominal overall concentration ($c_{\text{bulk, V}}$ =3.6 at%). This similarity indicates that the martensite decomposed into the α phase only to a negligible extent, despite the presence of the β phase in XRD (Fig. 7). At a VED of 357 J/mm^3 , the V content in the α phase was reduced (3.2 at%). However, this content was still significantly higher than that in the heat-treated sample (2.7 at%), which was close to the equilibrium solubility of V ($c_{\text{sol, V}}$ =2.6 at%) [52]. Thus, even the highest VED of 357 J/mm^3 did not bring the V content in the α phase to equilibrium. Correspondingly, the V content in the β phase exhibited a large variation for Ti-6Al-4V (12.8–28.6 at%) (Fig. 13 (b-2)), while the Mn content in the β phase showed limited variance for Ti-2Mn (11.5–14.9 at%) (Fig. 13 (a-2)). Therefore, this quantitative analysis of Mn and V partitioning clearly demonstrates the advantage of Ti-2Mn over Ti-6Al-4 V in promoting in-situ martensite decomposition, owing to its more favorable solute redistribution behavior.

3.4. Thermodynamic simulation

The previous sections revealed that Ti-2Mn exhibited the in-situ martensite decomposition more effectively than Ti-6Al-4V, evidenced by the microstructural evolution and solute partitioning. This facilitated decomposition can be attributed to two possible mechanisms: accelerated decomposition kinetics and enhanced thermodynamic stability of the β phase.

To evaluate the kinetic aspect, the evolution of the β phase from α′ martensite was simulated at 600 °C using a mobility database incorporating solute diffusivity (Fig. 14). In Ti-2Mn, the β volume fraction rapidly increased to 0.091 within 200 s and then stabilized. In contrast, Ti-6Al-4 V reached a similar final fraction of 0.099 only after more than 1200 s. These results indicate that Ti-2Mn attains a stable β volume fraction much more rapidly than Ti-6Al-4 V, demonstrating its accelerated martensite decomposition kinetics.

On the other hand, the thermodynamic aspect was assessed using the chemical driving force for martensite decomposition. Fig. 15 shows the

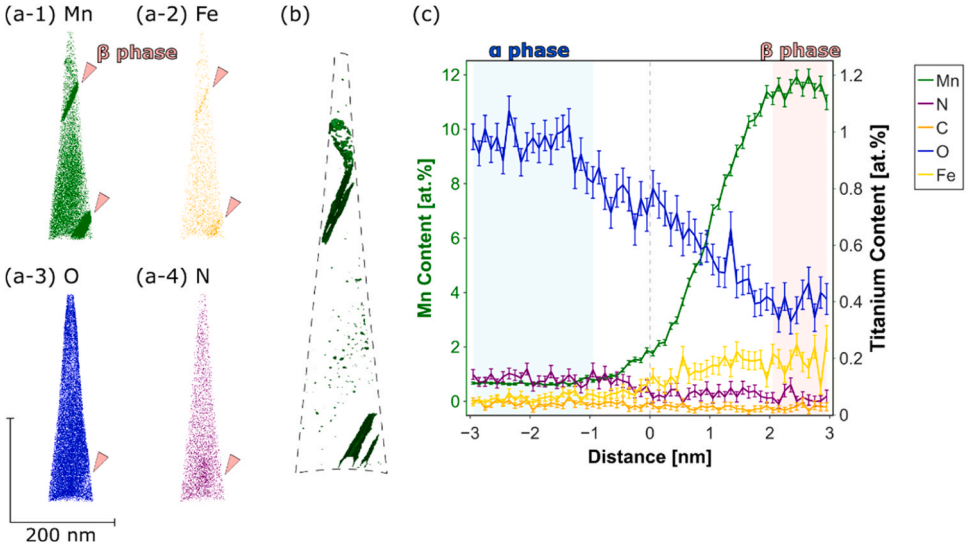

Fig. 12. APT analysis on Ti-2Mn built with the VED of 357 J/mm^3, including (a) 3D reconstructions of (1) Mn, (2) Fe, (3) O and (4) N of the analysed tip, (b) iso-concentration surface at 3 at% Mn, and (c) the proximity histogram.

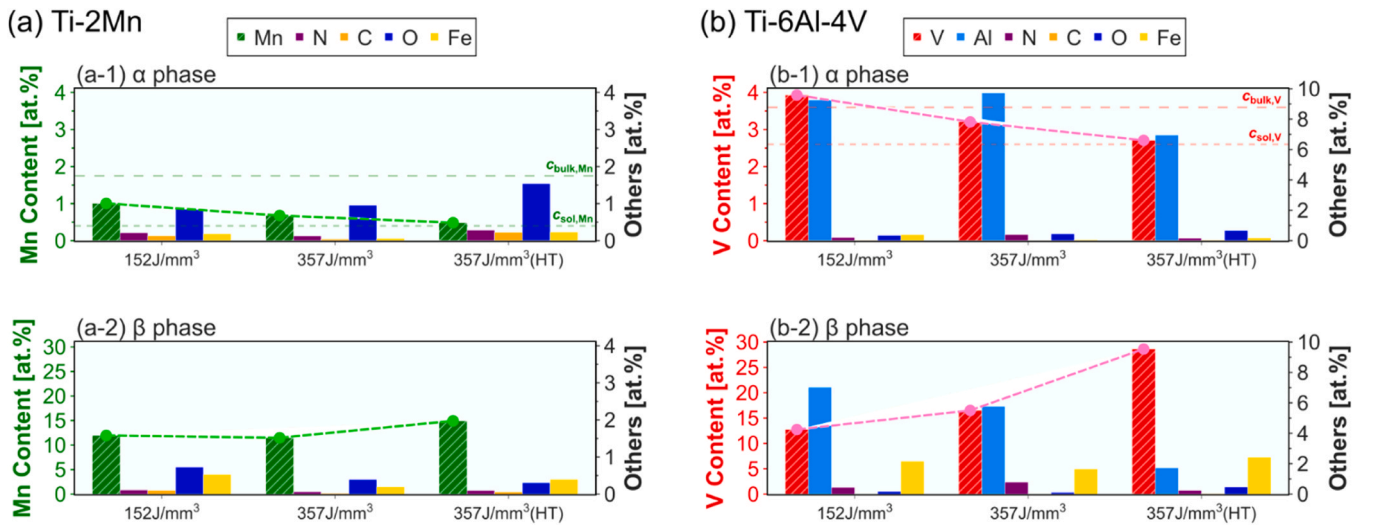

Fig. 13. Solute contents in (1) the α phase and (2) the β phase of (a) Ti-2Mn and (b) Ti-6Al-4V built with 152 and 357 J/mm^3. Note that HT refers to post heat treatment at 800℃ for 6 h.

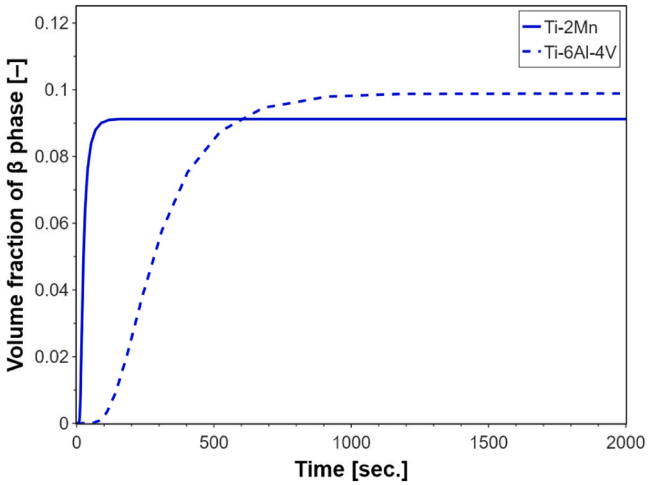

Fig. 14. Evolution of β phase volume fraction as a function of time for holding at 600℃.

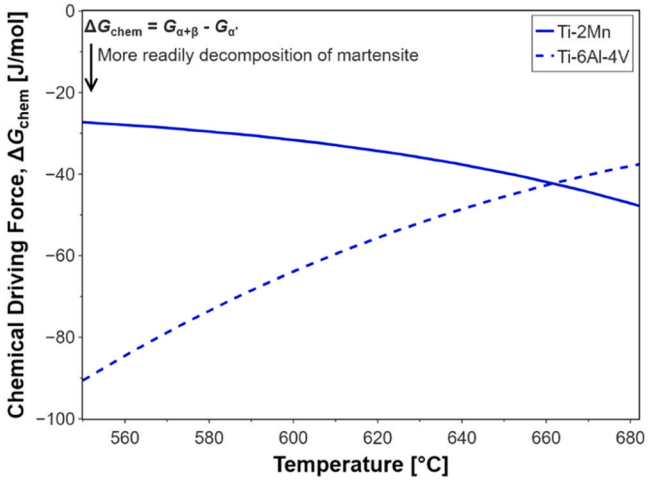

Fig. 15. Chemical driving force for martensite decomposition as a function of temperature for Ti-2Mn and Ti-6Al-4V.

driving force for Ti-2Mn and Ti-6Al-4 V within 550–682 °C, calculated from Eq. (1) using the Gibbs free energies of the α′ martensite and α+β phases (Fig. S2 in the supplementary material). This temperature range corresponds to the region of interest specified in Fig. 1. In both alloys, the driving force was negative, confirming that martensite decomposition is thermodynamically favourable. Moreover, Ti-6Al-4 V exhibited a more negative driving force over most of the temperature range, suggesting that Ti-6Al-4 V is thermodynamically more prone to martensite decomposition than Ti-2Mn.

Taken together, these thermodynamic and kinetic analyses indicate that Mn promotes martensite decomposition primarily through its high diffusivity rather than through thermodynamic stabilization of the β phase. This interpretation is consistent with our earlier CALPHAD-aided study [28], which identified Mn as an effective solute for accelerating martensite decomposition due to its high diffusivity.

3.5. Tensile properties

Because the Mn-facilitated martensite decomposition originates from its high diffusivity rather than β phase stabilization, this behaviour appears to be achievable only with a very limited set of fast-diffusing β stabilizers, such as Mn and Fe. Despite this unique characteristic of Mn, the mechanical properties of PBF–LB Ti-2Mn alloys have not yet been evaluated, whereas those of PBF–LB Ti-6Al-4 V have been widely reported [53]. Herein, to evaluate their potential as structural materials, their tensile properties were investigated. Furthermore, to understand the effect of in-situ martensite decomposition on mechanical performance, their tensile properties were compared between the VEDs of 152 and 357 J/mm^3.

Fig. 16 shows the nominal stress-strain curves of Ti-2Mn and Ti-6Al-4V built with the VEDs of 152 and 357 J/mm^3. Ti-2Mn exhibited greater ductility and lower strength than Ti-6Al-4V. Specifically, the mean ultimate tensile strength (UTS) of Ti-2Mn was 859 MPa at the VEDs of 357 J/mm^3, which were 28 % lower than those of Ti-6Al-4V (Table 1). A similar trend was observed at 152 J/mm^3, with a 23 % reduction. The higher strength of Ti-6Al-4V arises from the presence of an α phase strengthener (i.e., solid solution strengthening by Al).

This strength difference suggests limitations in positioning Ti-2Mn as a high-strength Ti alloy for structural applications. Nevertheless, Ti-2Mn still achieved approximately 2.5-times higher strength than as-built CP-Ti (UTS: 381 MPa) reported in the literature [49], while maintaining an elongation at fracture exceeding 10 %. Importantly, this level of ductility, which is often used as a benchmark for PBF–LB Ti

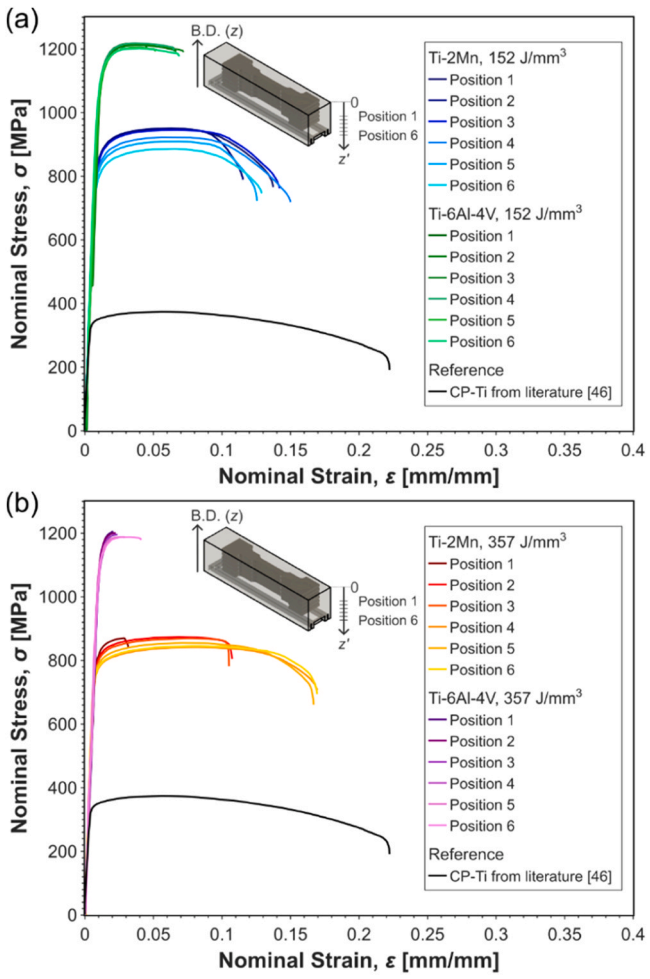

Fig. 16. Nominal tensile stress-strain curves of Ti-2Mn and Ti-6Al-4V built with (a) 152 and (b) 357 J/mm^3. The stress-strain curve of CP-Ti was taken from the literature [49].

Table 1
Means and 95 % confidence intervals of each tensile property calculated from the stress-strain curves of Ti-2Mn and Ti-6Al-4V in Fig. 16 [2]

	YS [MPa]	UTS [MPa]	Elongation at Fracture [%]	Uniform Elongation [%]
Ti-2Mn, 152 J/mm^3	815 ± 17	928 ± 19	13.3 ± 0.9	6.3 ± 0.2
Ti-2Mn, 357 J/mm^3	775 ± 13	857 ± 11	14.3 ± 2.7	7.8 ± 0.4
Ti-6Al-4V, 152 J/mm^3	1112 ± 18	1211 ± 4.9	6.1 ± 0.8	3.8 ± 0.1
Ti-6Al-4V, 357 J/mm^3	1131 ± 13	1194 ± 5.7	2.7 ± 0.5	2.5 ± 0.3

[2] The tensile properties of Position 1 in Ti-2Mn built with 357 J/mm^3 was excluded from the statistical calculation because of its exceptional fracture mode as shown in Fig. 18 (a).

alloys and corresponds to the lower limit of industrial standards for additively manufactured Ti-6Al-4 V [15,46,54], indicates that Ti-2Mn provides mechanically acceptable performance without requiring post-heat treatment.

Next, Table 1 and Fig. 17 compare the tensile properties of Ti-2Mn and Ti-6Al-4V between two VEDs. In both alloys, there were only

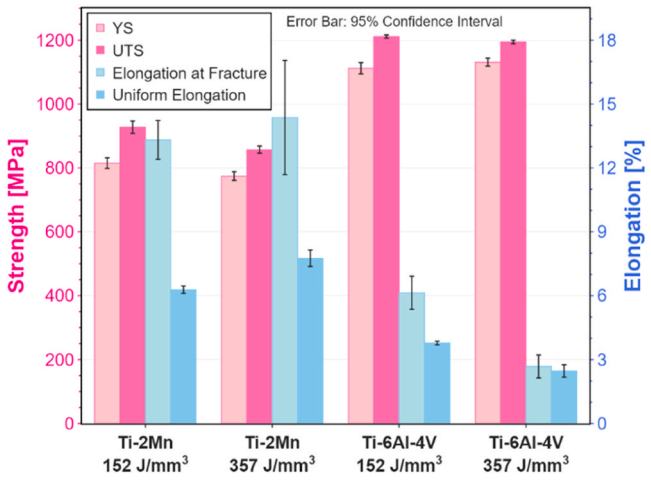

Fig. 17. Comparison of tensile properties of Ti-2Mn and Ti-6Al-4V between different VEDs: 152 and 357 J/mm^3.

marginal differences in yield strength (YS) and UTS. Although the largest difference was found in the UTS of Ti-2Mn, the strength reduction with increasing VED was limited to 8 %. Furthermore, the YS of Ti-2Mn and both the YS and UTS of Ti-6Al-4 V showed no significant differences between VEDs. These results indicate the in-situ martensite decomposition did not pronouncedly affect the strength, which is consistent with the previous reports [18,19,26].

Regarding the ductility, although Ti-2Mn did not exhibit the significant improvement in the elongation at fracture at the VED of 357 J/mm^3, their uniform elongation slightly increased from 6.3 % to 7.8 % (Table 1 and Fig. 17). In contrast, Ti-6Al-4V exhibit decreases in both elongation at fracture and uniform elongation at the VED of 357 J/mm^3. Note that the elongation at fracture in Ti-2Mn at the VED of 357 J/mm^3 exhibited a large confidence interval owing to the various fracture behaviours. As shown in Fig. 18 (a), there was a significantly large lack of fusion (LoF) on the fracture surface of the position 1. Furthermore, at the position 2, there was a limited reduction of area (15.6 %) (Fig. 18 (b)), while other specimens including the position 6 (357 J/mm^3) and the positions 1 and 6 (152 J/mm^3) showed the larger reduction of area (>40 %), exhibiting great local deformability (Fig. 18 (c-e)). The magnified micrographs of fracture surfaces showed a combination of dimples and facets in all specimens. However, there were no key features leading to the large variance of the elongation at fracture. Thus, the large confidence interval of the elongation at fracture stems from the difference in local deformability.

With regard to the effect of in-situ martensite decomposition on the ductility, Zafari et al. showed the large tensile elongation in the fully martensitic α' and fully decomposed α+β microstructures (~15 and ~12 %, respectively), in contrast to the significantly low elongation (<6 %) in the near-martensitic microstructures [18]. This ductility deterioration was considered due to the strain localisation around the thin β lath at isolated locations [18]. In the present study, Ti-2Mn predominantly exhibited the martensitic and decomposed microstructures at VEDs of 152 and 357 J/mm^3, respectively (Fig. 9). Thus, the consistently high elongation at fracture in Ti-2Mn aligns with this framework. Conversely, since Ti-6Al-4V showed the transition of microstructure into a near-martensitic type at high VED (Fig. 9), the reduced elongation is consistent with the idea of Zafari et al.

The improvement in uniform elongation of Ti-2Mn deserves further attention. According to Oh et al., the diffusion of β stabilizing elements (e.g., Mn and V) responsible for the martensite decomposition proceeds with the dislocation annihilation [44]. Since the multiplication and migration of dislocations accompany uniform deformation, a lower initial dislocation density facilitates higher uniform elongation. Thus, the martensite decomposition can increase uniform elongation. This

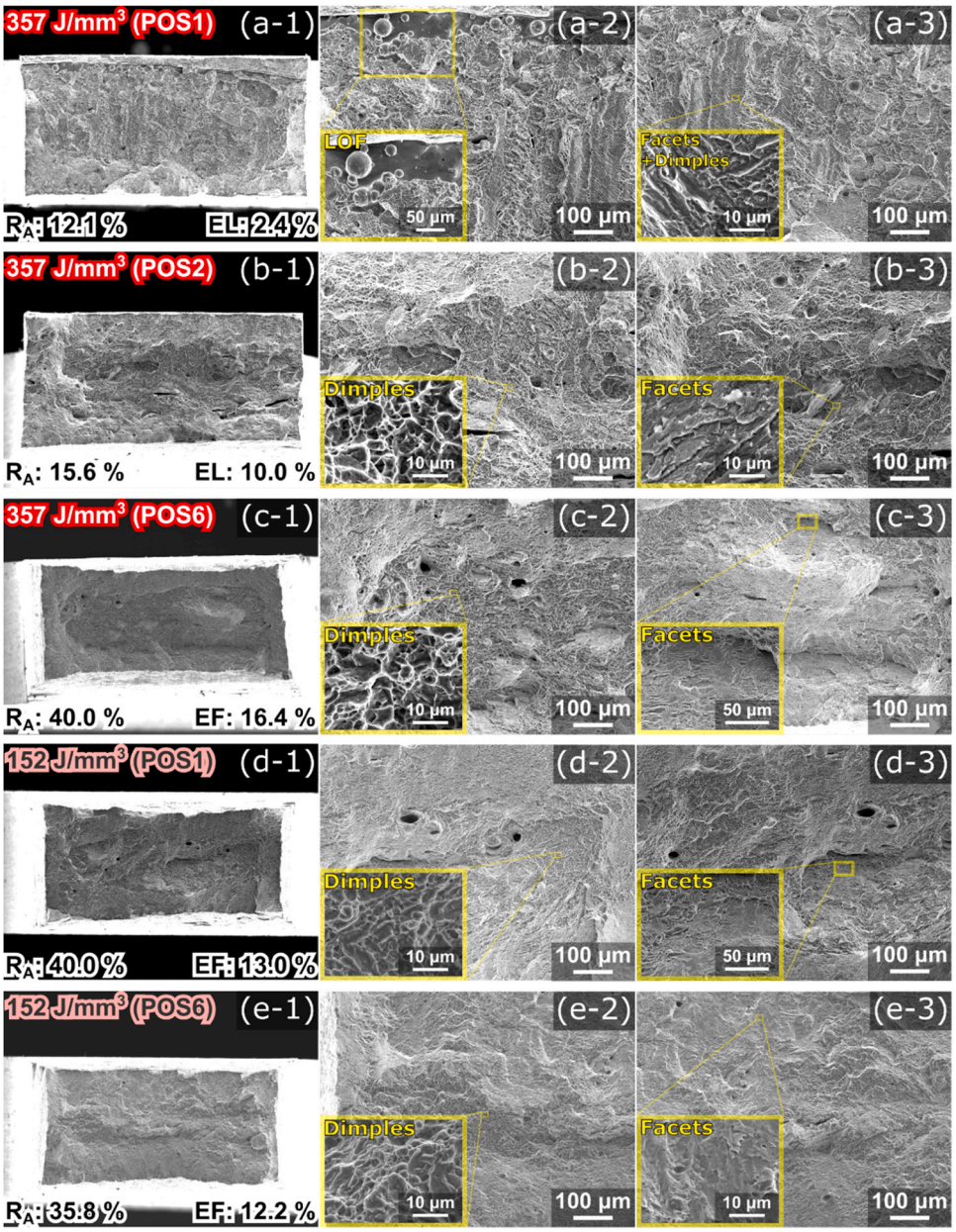

Fig. 18. Fracture surfaces at the different sampling positions of Ti-2Mn built with (a-c) 357 and (d-e) 152 J/mm^3, including micrographs with (1) low and (2,3) high magnifications. R_a and EF denoted in (1) indicate the reduction of area and elongation at fracture, respectively.

mechanism is further supported by literature showing increased necking strain in post-heat-treated α+β Ti alloys relative to as-built α′ alloys [55]. Accordingly, the improvement in uniform elongation observed in Ti-2Mn is reasonably attributed to in-situ martensite decomposition. In contrast, Ti-6Al-4V did not benefit from this mechanism because fracture occurred prematurely, before significant uniform deformation developed.

4. Conclusion

By applying an alloy-design approach for PBF–LB, the in-situ martensite decomposition of α+β Ti alloys was promoted. The as-built Ti-2Mn alloy, designed by leveraging Mn as a fast-diffusing β-stabilizer, exhibited the decomposition of α′ martensite into α+β microstructures at lower VEDs than Ti-6Al-4 V, despite comparable β-phase stability at the decomposition temperature. This evolution was accompanied by α-lattice expansion caused by the migration of β-stabilizing elements from the α to β phases. Specifically, in Ti-2Mn, the α phase achieved partial Mn depletion at 152 J/mm^3 and approached equilibrium Mn content at 357 J/mm^3 . In contrast, the V content in the α phase remained high at 152 J/mm^3 analogous to the nominal overall concentration, while reduced to only an intermediate level between the martensite and equilibrium state at 357 J/mm^3. The facilitated martensite decomposition in Ti-2Mn contributed to improved ductility; in particular, its uniform elongation increased from 6.3 % to 7.8 %. With regard to strength, only marginal differences in YS and UTS were observed between 152 and 357 J/mm^3 . Although Ti-2Mn exhibited lower strength than Ti-6Al-4 V, it still achieved approximately 2.5-times higher strength than as-built CP-Ti while maintaining sufficient ductility without post-heat treatment. These characteristics indicate that Ti-2Mn is not a high-strength alloy but rather a composition that offers practical advantages, including good processability and acceptable as-built mechanical performance. Overall, this study demonstrates that Mn addition provides a viable alloy-design strategy for

promoting the in-situ formation of α+β microstructures in PBF–LB Ti alloys, offering a complementary pathway to process-parameter-based microstructure control.

CRediT authorship contribution statement

Ammarueda Issariyapat: Writing – review & editing, Funding acquisition. **Jeff Huang:** Writing – review & editing, Methodology. **Delphine Chassaing:** Investigation. **Junko Umeda:** Supervision, Resources. **Katsuyoshi Kondoh:** Writing – review & editing, Supervision, Resources, Funding acquisition. **Michael Konrad Eusterholz:** Writing – review & editing, Resources, Methodology, Investigation. **Shota Kariya:** Resources. **Takuma Teramae:** Writing – original draft, Visualization, Project administration, Methodology, Investigation, Funding acquisition, Formal analysis, Data curation, Conceptualization. **Johannes Wild:** Writing – review & editing, Investigation, Formal analysis.

Declaration of Competing Interest

The authors declare the following financial interests/personal relationships which may be considered as potential competing interests: Takuma Teramae reports financial support was provided by Japan Science and Technology Agency. Katsuyoshi Kondoh reports financial support was provided by Japan Society for the Promotion of Science. Ammarueda Issariyapat reports financial support was provided by Japan Society for the Promotion of Science. If there are other authors, they declare that they have no known competing financial interests or personal relationships that could have appeared to influence the work reported in this paper.

Acknowledgements

This work was supported by JST university fellowships towards the Creation of Science and Technology Innovation (Grant Number: JPMJFS2125), the OU Master Plan Acceleration Project of the University of Osaka, and JSPS KAKENHI (Grant Number: 25K08345 and 25K17864). The APT analysis was carried out with the support of the Karlsruhe Nano Micro Facility (KNMFi, www.knmf.kit.edu) (Proposal-ID: 2024–032–032086). We are thankful to Marina Weinhard for supporting the specimen preparation for APT. Also, we would like to acknowledge Takeshi Murakami for his support with the TEM analysis and corresponding sample preparation.

Appendix A. Supporting information

Supplementary data associated with this article can be found in the online version at doi:10.1016/j.jallcom.2026.186733.

References

[1] M.H. Mosallanejad, A. Abdi, F. Karpasand, N. Nassiri, L. Iuliano, A. Saboori, Additive manufacturing of titanium alloys: processability, properties, and applications, Adv. Eng. Mater. 25 (2023) 2301122, https://doi.org/10.1002/adem.202301122.
[2] B. Sarzyński, L. Śnieżek, K. Grzelak, Metal additive manufacturing (MAM) applications in production of vehicle parts and components—a review, Metals 14 (2024) 195, https://doi.org/10.3390/met14020195.
[3] L.E. Murr, Global trends in the development of complex, personalized, biomedical, surgical implant devices using 3D printing/additive manufacturing: a review, Med Devices Sens 3 (2020) e10126, https://doi.org/10.1002/mds3.10126.
[4] E. Westphal, H. Seitz, Generative artificial intelligence: analyzing its future applications in additive manufacturing, BDCC 8 (2024) 74, https://doi.org/10.3390/bdcc8070074.
[5] M. Tebianian, S. Aghaie, N. Razavi Jafari, S. Elmi Hosseini, A. Pereira, F. Fernandes, M. Farbakhti, C. Chen, Y. Huo, A review of the metal additive manufacturing processes, Materials 16 (2023) 7514, https://doi.org/10.3390/ma16247514.
[6] J. Diller, C. Radlbeck, D. Siebert, J. Blankenhagen, D. Gubetini, F. Oberhaidinger, M. Mensinger, Additive Manufacturing in Construction—Implementing Powder-Bed Fusion of Metals Using a Laser (PBF-LB/M) and Shape Optimization in the Construction Design Process. INALCO 2023, MDPI, 2023, p. 10, https://doi.org/10.3390/engproc2023043010.
[7] P.A. Hooper, Melt pool temperature and cooling rates in laser powder bed fusion, Addit. Manuf. 22 (2018) 548–559, https://doi.org/10.1016/j.addma.2018.05.032.
[8] S. Liu, Y.C. Shin, Additive manufacturing of Ti6Al4V alloy: a review, Mater. Des. 164 (2019) 107552, https://doi.org/10.1016/j.matdes.2018.107552.
[9] T. Ahmed, H.J. Rack, Phase transformations during cooling in α +β titanium alloys, Mater. Sci. Eng. A 243 (1998) 206–211, https://doi.org/10.1016/S0921-5093(97)00802-2.
[10] C. Fleißner-Rieger, T. Pfeifer, C. Turk, H. Clemens, Optimization of the post-process heat treatment strategy for a near-α titanium base alloy produced by laser powder bed fusion, Materials 15 (2022) 1032, https://doi.org/10.3390/ma15031032.
[11] S. Cao, R. Chu, X. Zhou, K. Yang, Q. Jia, C.V.S. Lim, A. Huang, X. Wu, Role of martensite decomposition in tensile properties of selective laser melted Ti-6Al-4V, J. Alloy. Compd. 744 (2018) 357–363, https://doi.org/10.1016/j.jallcom.2018.02.111.
[12] X. Ji, H. Xie, J. Su, F. Jiang, J. Teng, H. Zhang, B. Guo, Phase transformation behaviors and dislocation evolutions of an additively manufactured Ti-6Al-4V alloy under annealing treatment, Metals 13 (2023) 1061, https://doi.org/10.3390/met13061061.
[13] J. Haubrich, J. Gussone, P. Barriobero-Vila, P. Kürnsteiner, E.A. Jägle, D. Raabe, N. Schell, G. Requena, The role of lattice defects, element partitioning and intrinsic heat effects on the microstructure in selective laser melted Ti-6Al-4V, Acta Mater. 167 (2019) 136–148, https://doi.org/10.1016/j.actamat.2019.01.039.
[14] M. Simonelli, Y.Y. Tse, C. Tuck, The formation of α + β microstructure in as-fabricated selective laser melting of Ti–6Al–4V, J. Mater. Res. 29 (2014) 2028–2035, https://doi.org/10.1557/jmr.2014.166.
[15] W. Xu, E.W. Lui, A. Pateras, M. Qian, M. Brandt, In situ tailoring microstructure in additively manufactured Ti-6Al-4V for superior mechanical performance, Acta Mater. 125 (2017) 390–400, https://doi.org/10.1016/j.actamat.2016.12.027.
[16] B. Farhang, A.A. Tanrikulu, A. Ganesh-Ram, S.H. Durlov, N. Shayesteh Moghaddam, Innovative fabrication design for in situ martensite decomposition and enhanced mechanical properties in laser powder bed fused Ti6Al4V alloy, JMMP 7 (2023) 226, https://doi.org/10.3390/jmmp7060226.
[17] P. Barriobero-Vila, J. Gussone, J. Haubrich, S. Sandlöbes, J. Da Silva, P. Cloetens, N. Schell, G. Requena, Inducing stable α + β microstructures during selective laser melting of Ti-6Al-4V using intensified intrinsic heat treatments, Materials 10 (2017) 268, https://doi.org/10.3390/ma10030268.
[18] A. Zafari, M.R. Barati, K. Xia, Controlling martensitic decomposition during selective laser melting to achieve best ductility in high strength Ti-6Al-4V, Materials Science Engineering A 744 (2019) 445–455, https://doi.org/10.1016/j.msea.2018.12.047.
[19] L.L. Xing, W.J. Zhang, C.C. Zhao, W.Q. Gao, Z.J. Shen, W. Liu, Influence of powder bed temperature on the microstructure and mechanical properties of Ti-6Al-4V alloy fabricated via laser powder bed fusion, Materials 14 (2021) 2278, https://doi.org/10.3390/ma14092278.
[20] G.M. Ter Haar, T.H. Becker, Laser powder bed fusion produced Ti-6Al-4V: Influence of high-energy process parameters on in-situ martensite decomposition and prior beta grain texture, J. Alloy. Compd. 918 (2022) 165497, https://doi.org/10.1016/j.jallcom.2022.165497.
[21] F. Nahr, T. Novotny, D. Kunz, U. Kleinhans, L. Chechik, D. Bartels, M. Schmidt, Advanced process control in laser-based powder bed fusion–Smart Fusion feedback-loop control as a path to uniform properties for complex structures? J. Mater. Res. Technol. 34 (2025) 604–618, https://doi.org/10.1016/j.jmrt.2024.12.014.
[22] A.E. Medvedev, S. Brudler, S. Piegert, T. Illston, M. Qian, M. Brandt, Interlayer time as a robust, geometry-agnostic predictor of microstructural and mechanical properties evolution in PBF-LB/M Ti6Al4V alloy, J. Mater. Process. Technol. 340 (2025) 118858, https://doi.org/10.1016/j.jmatprotec.2025.118858.
[23] S. Dhiman, V. Chinthapenta, M. Brandt, D. Fabijanic, W. Xu, Microstructure control in additively manufactured Ti-6Al-4V during high-power laser powder bed fusion, Addit. Manuf. 96 (2024) 104573, https://doi.org/10.1016/j.addma.2024.104573.
[24] Z. Liu, Q. Zhou, X. Liang, X. Wang, G. Li, K. Vanmeensel, J. Xie, Alloy design for laser powder bed fusion additive manufacturing: a critical review, Int. J. Extrem. Manuf. 6 (2024) 022002, https://doi.org/10.1088/2631-7990/ad1657.
[25] H.R. Kotadia, G. Gibbons, A. Das, P.D. Howes, A review of laser powder bed fusion additive manufacturing of aluminium alloys: microstructure and properties, Addit. Manuf. 46 (2021) 102155, https://doi.org/10.1016/j.addma.2021.102155.
[26] J. Zhang, Y. Liu, G. Sha, S. Jin, Z. Hou, M. Bayat, N. Yang, Q. Tan, Y. Yin, S. Liu, J. H. Hattel, M. Dargusch, X. Huang, M.-X. Zhang, Designing against phase and property heterogeneities in additively manufactured titanium alloys, Nat. Commun. 13 (2022) 4660, https://doi.org/10.1038/s41467-022-32446-2.
[27] L. Scotti, N. Warnken, A. Mottura, Non-classical interstitial sites and anomalous diffusion mechanisms in hcp-titanium, Acta Mater. 177 (2019) 68–81, https://doi.org/10.1016/j.actamat.2019.07.023.
[28] T. Teramae, A. Issariyapat, S. Kariya, J. Umeda, K. Kondoh, Exploring β stabilizing elements of α+β Ti-Al alloys for facilitating in-situ martensite decomposition in PBF-LB, J. Jpn. Soc. Powder Powder Metall. 72 (2025) 201–209, https://doi.org/10.2497/jjspm.25-00020.
[29] T. Abe, K. Hashimoto, Y. Goto, Y. Sawada, K. Hirose, CPDDB, (2007). https://doi.org/10.48505/NIMS.3060.
[30] A.U. Khan, P. Brož, M. Premović, J. Pavlů, J. Vřeštál, X. Yan, D. Maccio, A. Saccone, G. Giester, P. Rogl, The Ti–Mn system revisited: experimental investigation and thermodynamic modelling, Phys. Chem. Chem. Phys. 18 (2016) 23326–23339, https://doi.org/10.1039/C6CP04542A.

[31] S.-L. Chen, S. Daniel, F. Zhang, Y.A. Chang, X.-Y. Yan, F.-Y. Xie, R. Schmid-Fetzer, W.A. Oates, The PANDAT software package and its applications, Calphad 26 (2002) 175–188, https://doi.org/10.1016/S0364-5916(02)00034-2.
[32] Z. Song, Y. Liu, J. Wang, G. Zhu, L. Wang, X. Zeng, M. Knezevic, Advanced phenomenological models guided heat treating processes for LPBF Ti-6Al-4V alloy, Mater. Today Commun. 42 (2025) 111186, https://doi.org/10.1016/j.mtcomm.2024.111186.
[33] J.L. Murray, The Mn−Ti (Manganese-Titanium) system, Bull. Alloy Phase Diagr. 2 (1981) 334–343, https://doi.org/10.1007/BF02868287.
[34] W. Cao, F. Zhang, K. Kadirvel, S. Chen, E. Payton, M. Krug, Panevolution: integrating calphad, microstructure modeling, and finite element method, Calphad 90 (2025) 102851, https://doi.org/10.1016/j.calphad.2025.102851.
[35] N. Sridharan, Y. Chen, P. Nandwana, R.M. Ulfig, D.J. Larson, S.S. Babu, On the potential mechanisms of β to α'+ β decomposition in two phase titanium alloys during additive manufacturing: a combined transmission Kikuchi diffraction and 3D atom probe study, J. Mater. Sci. 55 (2020) 1715–1726, https://doi.org/10.1007/s10853-019-03984-w.
[36] R. Shi, N. Ma, Y. Wang, Predicting equilibrium shape of precipitates as function of coherency state, Acta Mater. 60 (2012) 4172–4184, https://doi.org/10.1016/j.actamat.2012.04.019.
[37] S. Wang, T. Wen, J. Han, D.J. Srolovitz, Coherent and semicoherent α/β interfaces in titanium: structure, thermodynamics, migration, npj Comput. Mater. 9 (2023) 216, https://doi.org/10.1038/s41524-023-01170-w.
[38] W.H. Kan, M. Gao, X. Zhang, E. Liang, N.S.L. Chiu, C.V.S. Lim, A. Huang, The influence of porosity on Ti-6Al-4V parts fabricated by laser powder bed fusion in the pursuit of process efficiency, Int J. Adv. Manuf. Technol. 119 (2022) 5417–5438, https://doi.org/10.1007/s00170-021-08374-8.
[39] C.A. Schneider, W.S. Rasband, K.W. Eliceiri, NIH Image to ImageJ: 25 years of image analysis, Nat. Methods 9 (2012) 671–675, https://doi.org/10.1038/nmeth.2089.
[40] J.M.S. Prewitt, M.L. Mendelsohn, The analysis of cell images, Ann. N. Y. Acad. Sci. 128 (1966) 1035–1053, https://doi.org/10.1111/j.1749-6632.1965.tb11715.x.
[41] N. Doebelin, R. Kleeberg, *Profex*: a graphical user interface for the Rietveld refinement program *BGMN*, J. Appl. Crystallogr 48 (2015) 1573–1580, https://doi.org/10.1107/S1600576715014685.
[42] A. Vaitkus, A. Merkys, T. Sander, M. Quirós, P.A. Thiessen, E.E. Bolton, S. Gražulis, A workflow for deriving chemical entities from crystallographic data and its application to the Crystallography Open Database, J. Chemin.. 15 (2023) 123, https://doi.org/10.1186/s13321-023-00780-2.
[43] A. Savitzky, M.J.E. Golay, Smoothing and differentiation of data by simplified least squares procedures, Anal. Chem. 36 (1964) 1627–1639, https://doi.org/10.1021/ac60214a047.
[44] S.A. Oh, J.W. Aroh, N.L. Lamprinakos, C.A. Chuang, A.N. Bucsek, A.D. Rollett, Martensite decomposition during rapid heating of Ti-6Al-4V studied via in situ synchrotron X-ray diffraction, Commun. Mater. 5 (2024) 58, https://doi.org/10.1038/s43246-024-00492-6.
[45] Z.-H. Yu, S. Cao, R. Yang, Q.-M. Hu, Enhanced solid solution hardening by off-center substitutional solute atoms in α-Ti, Mater. Des. 251 (2025) 113709, https://doi.org/10.1016/j.matdes.2025.113709.
[46] J. Huang, A. Issariyapat, S. Kariya, J. Umeda, K. Kondoh, On the viability of in-situ alloyed Ti-1Fe as a strong and ductile alternative to Ti-6Al-4V for laser-based powder bed fusion, Addit. Manuf. 105 (2025) 104788, https://doi.org/10.1016/j.addma.2025.104788.
[47] P. Mwangi, A. Otsu, Z.-C. Chen, First-principles calculations on the effect of interstitial oxygen on structural, thermodynamic, and elastic properties of titanium-oxygen alloys, Comput. Mater. Sci. 246 (2025) 113405, https://doi.org/10.1016/j.commatsci.2024.113405.
[48] A. Issariyapat, S. Kariya, K. Shitara, J. Umeda, K. Kondoh, Solute-induced near-isotropic performance of laser powder bed fusion manufactured pure titanium, Addit. Manuf. 56 (2022) 102907, https://doi.org/10.1016/j.addma.2022.102907.
[49] E. Ichikawa, K. Shitara, J. Umeda, S. Li, B. Chen, K. Kondoh, Microstructures and strengthening mechanism of oxygen soluted titanium by selective laser melting, J. Jpn. Soc. Powder Powder Metall. 68 (2021) 67–75, https://doi.org/10.2497/jjspm.68.67.
[50] A. Fitzner, D.G.L. Prakash, J.Q. Da Fonseca, M. Thomas, S.-Y. Zhang, J. Kelleher, P. Manuel, M. Preuss, The effect of aluminium on twinning in binary alpha-titanium, Acta Mater. 103 (2016) 341–351, https://doi.org/10.1016/j.actamat.2015.09.048.
[51] P.V. Cobbinah, S. Matsunaga, Y. Toda, R. Ozasa, M. Okugawa, T. Ishimoto, Y. Liu, Y. Koizumi, P. Wang, T. Nakano, Y. Yamabe-Mitarai, Peculiar microstructural evolution and hardness variation depending on laser powder bed fusion-manufacturing condition in Ti–6Al–2Sn–4Zr–6Mo, Smart Mater. Manuf. 2 (2024) 100050, https://doi.org/10.1016/j.smmf.2024.100050.
[52] J.L. Murray, The Ti−V (Titanium-Vanadium) system, Bull. Alloy Phase Diagr. 2 (1981) 48–55, https://doi.org/10.1007/BF02873703.
[53] H.D. Nguyen, A. Pramanik, A.K. Basak, Y. Dong, C. Prakash, S. Debnath, S. Shankar, I.S. Jawahir, S. Dixit, D. Buddhi, A critical review on additive manufacturing of Ti-6Al-4V alloy: microstructure and mechanical properties, J. Mater. Res. Technol. 18 (2022) 4641–4661, https://doi.org/10.1016/j.jmrt.2022.04.055.
[54] ASTM International F42 Committee, Specification for Additive Manufacturing Titanium-6 Aluminum-4 Vanadium with Powder Bed Fusion, (2014). https://doi.org/10.1520/F2924-14.
[55] C. Xuan, A study of microstructural factors governing strength and ductility of titanium alloys fabricated by powder bed fusion additive manufacturing, J. Alloy. Compd. 952 (2023) 170094, https://doi.org/10.1016/j.jallcom.2023.170094.